J. Marine Sci. Appl. (2017) 16: 417-426
DOI: https://doi.org/10.1007/s11804-017-1435-5

Numerical Computation of Motions and Structural Loads for Large Containership using 3D Rankine Panel Method

Jung-Hyun Kim and Yonghwan Kim*

Department of Naval Architecture & Ocean Engineering, Seoul National University, Seoul 08826, Korea

Abstract: In this paper, we present the results of our numerical seakeeping analyses of a 6750-TEU containership, which were subjected to the benchmark test of the 2nd ITTC–ISSC Joint Workshop held in 2014. We performed the seakeeping analyses using three different methods based on a 3D Rankine panel method, including 1) a rigid-body solver, 2) a flexible-body solver using a beam model, and 3) a flexible-body solver using the eigenvectors of a 3D Finite Element Model (FEM). The flexible-body solvers adopt a fully coupled approach between the fluid and structure. We consider the nonlinear Froude–Krylov and restoring forces using a weakly nonlinear approach. In addition, we calculate the slamming loads on the bow flare and stern using a 2D generalized Wagner model. We compare the numerical and experimental results in terms of the linear response, the time series of the nonlinear response, and the longitudinal distribution of the sagging and hogging moments. The flexible-body solvers show good agreement with the experimental model with respect to both the linear and nonlinear results, including the high-frequency oscillations due to springing and whipping vibrations. The rigid-body solver gives similar results except for the springing and whipping.
Keywords: Rankine panel method, fluid-structure interaction, benchmark test, containership, springing, whipping

Article ID: 1671-9433(2017)04-0417-10

1 Introduction

For many years, potential flow has been used as the basis of seakeeping analysis methods. Initially, 2D methods such as the slender-body and strip theories attracted enormous attention from researchers and designers (Korvin-Kroukovsky and Jacobs, 1957; Newman, 1964; Ogilvie and Tuck, 1969; Salvesen *et al*., 1970). To overcome the limitations of the 2D methods, 3D boundary element methods (BEM) were later developed, which use either a wave Green's function or a Rankine source as the source potential. The wave analysis program developed at MIT (WAMIT) is a very well-known program that uses a wave Green's function in the frequency domain (Korsmeyer *et al*., 1988). Ship wave analyses (Nakos and Sclavounos, 1990; Kring, 1994) and the Large Amplitude Motions Program (Lin and Yue, 1991) comprise another set of well-known programs that use a Rankine source in the time domain. Bishop and Price (1979) proposed a 2D hydroelastic analysis method for seakeeping analysis that takes into account linear springing vibrations, based on the strip and Timoshenko beam theories. Jensen and Dogliani (1996) proposed a quadratic strip theory for second-order springing. Malenica and Tuitman (2008) proposed a 3D hydroelastic method for springing and whipping vibrations. Hirdaris and Temarel (2009) summarized the recent advances and future trends of the hydroelastic method. Computational Fluid Dynamics (CFD) methods have also been also employed for seakeeping analysis (Gentaz *et al*., 1999; Sadat-Hosseini *et al*., 2013; Yang *et al*., 2013).

There are many seakeeping analysis programs worldwide, but it is difficult to decide which program to use without comparing their results. A benchmark test could be useful for providing reliable comparative data. The ITTC committee conducted a comparative study on ship motions and loads for the S175 containership (ITTC, 1978), for which the respective codes were based on strip theories. Another comparative study on the S175 containership was performed in 2010 by one of the authors of this study as part of an ITTC workshop on seakeeping. Cooperative Research Ships also conducted a comparative containership study (Bunnik *et al*., 2010). A benchmark test on the motions and loads of a 6750-TEU containership was performed as part of the 2nd ITTC–ISSC Joint Workshop in 2014 (Kim and Kim, 2016). In the latter three studies, the results were obtained by using and then comparing the results of various seakeeping analysis methods. Seoul National University (SNU) participated in the benchmark test of the 6750-TEU containership by the development and use of WISH computer programs that are based on a 3D Rankine panel method for seakeeping analysis (Kim *et al*., 2011). In this paper, we discuss the theoretical background, numerical model, and results of the WISH programs, which include rigid-body and flexible-body solvers based on either a beam theory or the eigenvectors of s 3D Finite Element Model (FEM). We compare the motion and load responses generated by different solvers with experimental results and

Received date: 06-Dec-2016
Accepted date: 06-May-2017
Foundation item: Supported by Lloyd's Register Foundation (LRF)-Funded Research Center at SNU (LRFC)
***Corresponding author Email:** yhwankim@snu.ac.kr

The original paper was presented in the First International Conference on Naval Architecture and Ocean Engineering (NAOE 2016, Saint-Petersburg)

discuss the requirements of flexible-body solvers.

2 Theoretical background

We used three seakeeping analysis codes—WISH, WISH-FLEX BEAM, and WISH-FLEX 3DM—in our seakeeping test simulations. Table 1 compares these codes. WISH, which was developed as the core program, is a rigid-body motion solver based on a 3D Rankine panel method. We developed the WISH-FLEX BEAM code by coupling WISH and a beam-based motion solver (Kim *et al*., 2009) and we developed the WISH-FLEX 3DM code by coupling WISH with eigenvectors of the 3D FEM (Kim and Kim, 2014). The WISH-FLEX codes adopt a fully coupled approach and support the simulation of springing and slamming–whipping. We compared the results of the WISH-FLEX codes with those of other numerical methods and experiments provided in previous work (Kim and Kim, 2014; Shin *et al.*, 2016).

Table 1 Comparison of analysis codes based on the 3D Rankine panel method

Code name	WISH	WISH-FLEX BEAM	WISH-FLEX 3DM
Fluid domain	3D Rankine panel method		
Structural domain	Rigid-body	Beam approximation	Eigenvectors of 3D FEM
Slamming model	Not supported	2D wedge approximation/ 2D generalized Wagner model	

2.1 3D Rankine panel method

The fluid flow surrounding a ship structure is assumed to be a potential flow, and we can use a 3D Rankine panel method to obtain a solution for the potential flow. The numerical implementation of this solution is based on the works of Kim and Kim (2008), Kring (1994), and Nakos and Sclavounos (1990).

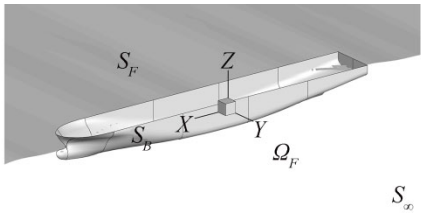

Fig. 1 Coordinate system of 3D Rankine panel method

The coordinate system moves with the advancing ship, as shown in Fig. 1, and the origin is located at the projection of the center of mass on the water plane. A set of equations for a boundary value problem can be expressed as follows:

$$\nabla^2\phi = 0 \quad \text{in } \Omega_F \tag{1}$$

$$\frac{\partial \phi}{\partial n} = \boldsymbol{U}\cdot\boldsymbol{n} + \frac{\partial \boldsymbol{u}}{\partial t}\cdot\boldsymbol{n} \quad \text{on } S_B \tag{2}$$

$$\left[\frac{\mathrm{d}}{\mathrm{d}t} + \nabla\phi\cdot\nabla\right]\left[z-\zeta(x,y,t)\right] = 0 \text{ on } z=\zeta(x,y,t) \tag{3}$$

$$\frac{\mathrm{d}\phi}{\mathrm{d}t} = -g\zeta - \frac{1}{2}\nabla\phi\cdot\nabla\phi \quad \text{on } z=\zeta(x,y,t) \tag{4}$$

$$\nabla\phi = 0 \quad \text{at } S_\infty \tag{5}$$

where ϕ is the velocity potential, $\boldsymbol{U}$ is the forward speed vector, $\boldsymbol{n}$ is the normal vector on the body surface, $\boldsymbol{u}$ is the translational displacement vector, S_B is the body surface, Ω_F is the fluid domain, ζ is the free surface elevation, and g is the gravitational acceleration.

To linearize the boundary conditions of Eqs. (2)–(4), we decompose the velocity potential into the double-body basis potential Φ, the incident potential ϕ_I, and the disturbed potential ϕ_d. In the same manner, we decompose the free surface elevation into the incident wave elevation ζ_I and the disturbed wave elevation ζ_d. We then lineraize Eqs. (2)–(4) at the mean position using Taylor series expansion, as follows:

$$\frac{\partial\zeta_d}{\partial t} - (\boldsymbol{U}-\nabla\Phi)\cdot\nabla\zeta_d = \frac{\partial^2\Phi}{\partial z^2}\zeta_d + \frac{\partial\phi_d}{\partial z} + (\boldsymbol{U}-\nabla\Phi)\cdot\nabla\zeta_I \quad \text{on } z=0 \tag{6}$$

$$\frac{\partial\phi_d}{\partial t} - (\boldsymbol{U}-\nabla\Phi)\cdot\nabla\phi_d = -\frac{\partial\Phi}{\partial t} - g\zeta_d + \left[\boldsymbol{U}\cdot\nabla\Phi - \frac{1}{2}\nabla\Phi\cdot\nabla\Phi\right] + (\boldsymbol{U}-\nabla\Phi)\cdot\nabla\phi_I \text{ on } z=0 \tag{7}$$

$$\frac{\partial\phi_d}{\partial n} = \left[(\boldsymbol{u}\cdot\nabla)(\boldsymbol{U}-\nabla\Phi) + ((\boldsymbol{U}-\nabla\Phi)\cdot\nabla)\boldsymbol{u}\right]\cdot\boldsymbol{n} + \frac{\partial\boldsymbol{u}}{\partial t}\cdot\boldsymbol{n} - \frac{\partial\phi_I}{\partial n} \quad \text{on } \bar{S}_B \tag{8}$$

All the terms of Eqs. (6)–(8) are in the order $\varepsilon(<<1)$. Using the form presented by Ogilvie and Tuck (1969), we modify the body boundary condition of Eq. (8) as follows:

$$\frac{\partial\phi_d}{\partial n} = \sum_{j=1}^{n}\left(\frac{\partial\xi_j}{\partial t}n_j + \xi_j m_j\right) - \frac{\partial\phi_I}{\partial n} \quad \text{on } \bar{S}_B$$
$$n_j = \boldsymbol{A}^j\cdot\boldsymbol{n}, \quad m_j = (\boldsymbol{n}\cdot\nabla)(\boldsymbol{A}^j\cdot(\boldsymbol{U}-\nabla\Phi)) \tag{9}$$

where $\boldsymbol{A}^j$ is the eigenvector of the jth mode and m_j is the so-called m term. Once we have determined the boundary values, we can obtain the velocity potential using the following equation:

$$\phi_d + \iint_{S_B}\phi_d\frac{\partial G}{\partial n}\mathrm{d}S - \iint_{S_F}\frac{\partial\phi_d}{\partial n}G\mathrm{d}S = \iint_{S_B}\frac{\partial\phi_d}{\partial n}G\mathrm{d}S - \iint_{S_F}\phi_d\frac{\partial G}{\partial n}\mathrm{d}S \tag{10}$$

where G is the Rankine source term. We derive Eq. (10) from the Laplace equation and Green's second identity. We then evaluate the boundary values on the discretized panels and interpolate them using a bi-quadratic spline function. Once we obtain the velocity potential by solving Eq. (10), we can calculate the dynamic pressure using the Bernoulli equation. In addition, we adopt a weakly nonlinear approach

to consider nonlinear the Froude–Krylov and restoring forces. The explicit forms of the dynamic and static pressures have been provided by Kim and Kim (2014).

2.2 2D generalized Wagner model

To consider the slamming loads on the bow flare and stern, we apply a 2D Generalized Wagner Model (GWM) to water-entry events. We use a space-fixed coordinate system whose origin is located at the intersection of the vertical axis of symmetry and the free surface of the calm water, as shown in Fig. 2. In this study, the solution is limited to a symmetric water-entry problem without any flow separation. A set of equations for the initial value problem is expressed as follows (Zhao *et al*., 1996; Khabakhpasheva *et al*., 2014):

$$\nabla^2\varphi = 0 \tag{11}$$

$$\varphi = 0 \quad (y = H(t)) \tag{12}$$

$$S_t(x,t) = \varphi_y(x,H(t),t) \quad (|x| > c(t)) \tag{13}$$

$$\varphi_y = f'(x)\varphi_x - \dot{h}(t) \quad (y = f(x) - h(t),\ |x| < c(t)) \tag{14}$$

$$\varphi \to 0 \quad (x^2+y^2 \to \infty) \tag{15}$$

$$H(t) = f(c(t)) - h(t) \tag{16}$$

$$S(x,0) = 0, \quad c(0) = 0 \tag{17}$$

where φ is the velocity potential of GWM; $H(t)$ is the free surface elevation at the contact point defined as $H(t) = S[c(t),t]$; $S(x,t)$ is the free surface elevation; subscripts x, y, and t denote partial derivatives with respect to their values; $f'(x)$ is the slope of the body geometry; $\dot{h}(t)$ is the relative vertical velocity of the body and free surface; and $c(t)$ is the *x*-coordinate at the contact. We then solve the initial boundary value problem using conformal mapping, according to the work of Khabakhpasheva *et al*. (2014). We express the final pressure distribution as follows:

$$p = \rho\dot{h}^2 P_v(\xi,c) + \rho\ddot{h}P_w(\xi,c) \tag{18}$$

$$\begin{aligned} P_v(\xi,c) = {} & \frac{X_c(\xi,c)}{N(c)}\frac{\xi}{S(\xi,c)}(1-\xi)^{-k(c)} - \\ & \frac{0.5}{1+f_x^2(X)}\frac{\xi^2}{S^2(\xi,c)}(1-\xi)^{-2k(c)} + \\ & \frac{F'_\infty(c)}{N(c)}\sqrt{1-\xi^2} + \frac{1}{2} - \frac{f_x(c)}{N(c)} \end{aligned} \tag{19}$$

$$P_w(\xi,c) = f(X) - f(c) + F_\infty(c)\sqrt{1-\xi^2} \tag{20}$$

where ρ is the water density, ξ is the x-coordinate on the wetted body surface normalized by c, $F_\infty(c)$ is the coefficient in the far-field asymptotic of the conformal mapping, and $N(c)$, $f(X)$, and $f(c)$ are functions from the Wagner equation. Using offsets in the splash-up of the free surface, we can relate a preprocessed solution based on a zero initial condition to other water-entry events with nonzero initial conditions. This approach is adequate because the gravity term is neglected in the free surface boundary condition, which implies that the splash-up depends on the vertical displacement of the current. Thus, we used the preprocessed solution to evaluate slamming loads in the seakeeping analysis (Kim *et al*., 2015).

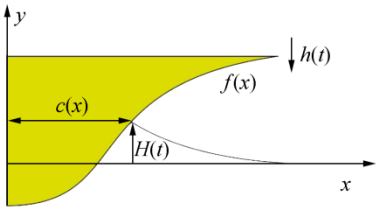

Fig. 2 Coordinate system of 2D generalized Wagner model

2.3 Rigid-body approximation

Rigid-body approximation is a classical approach for approximating the structure of a ship. It can be interpreted from the viewpoint of modal decomposition as follows. Once the ship structure is discretized into nodes in a Cartesian coordinate system, the equation of motion can be expressed in terms of matrices and vectors as follows:

$$\boldsymbol{M}\ddot{\boldsymbol{u}}(t) + \boldsymbol{C}\dot{\boldsymbol{u}}(t) + \boldsymbol{K}\boldsymbol{u}(t) = \boldsymbol{f}(\ddot{\boldsymbol{u}}(t),\dot{\boldsymbol{u}}(t),\boldsymbol{u}(t),t) \tag{21}$$

where $\boldsymbol{M}$ is the mass matrix, $\boldsymbol{C}$ is the damping matrix, $\boldsymbol{K}$ is the stiffness matrix, $\boldsymbol{u}(t)$ is the displacement vector of six DOFs, the dot over the vector represents the time derivative, and $\boldsymbol{f}$ is the external force vector. The displacement vector of the body can be decomposed into each component of eigenvectors as follows:

$$\begin{aligned} \boldsymbol{u}(t) = \sum_{j=1}^{6*m}\alpha^j(t)\boldsymbol{A}^j \approx \sum_{j=1}^{n}\alpha^j(t)\boldsymbol{A}^j = \\ \left[\boldsymbol{A}^1\boldsymbol{A}^2\cdots\boldsymbol{A}^n\right]\left\{\alpha^{1\sim n}(t)\right\} = \boldsymbol{u}'(t) \end{aligned} \tag{22}$$

where $\boldsymbol{u}'(t)$ is the approximated displacement vector, α^j is the modal displacement of the *j*th mode, $\boldsymbol{A}^j$ is the eigenvector of the *j*th mode, *m* is the total number of nodes, and *n* is the sufficient number of lower modes, which satisfies Eq. (22). By multiplying Eq. (21) by the transpose of the eigenvector matrix and substituting Eq. (22) into Eq. (21), we obtain the equation of motion as follows:

$$\begin{aligned} & \begin{bmatrix} \boldsymbol{M}_L & 0 \\ 0 & \boldsymbol{M}_H \end{bmatrix}\begin{Bmatrix} \ddot{\alpha}^{1\sim n}(t) \\ \ddot{\alpha}^{n\sim}(t) \end{Bmatrix} + \begin{bmatrix} \boldsymbol{C}_L & 0 \\ 0 & \boldsymbol{C}_H \end{bmatrix}\begin{Bmatrix} \dot{\alpha}^{1\sim n}(t) \\ \dot{\alpha}^{n\sim}(t) \end{Bmatrix} + \\ & \begin{bmatrix} \boldsymbol{K}_L & 0 \\ 0 & \boldsymbol{K}_H \end{bmatrix}\begin{Bmatrix} \alpha^{1\sim n}(t) \\ \alpha^{n\sim}(t) \end{Bmatrix} \approx \left\{f^{1\sim}(\ddot{u}'(t),\dot{u}'(t),u'(t),t)\right\} \end{aligned} \tag{23}$$

where subscripts *L* and *H* of the modal matrices indicate the lower and higher modes, respectively, and $f^{1\sim}$ is the modal external force. If the ship structure is assumed to be rigid, Eq. (23) is reduced to the following:

$$\boldsymbol{M}_L\left\{\ddot{\alpha}^{1\sim 6}(t)\right\} = \left\{f^{1\sim 6}(\ddot{u}'(t),\dot{u}'(t),u'(t),t)\right\} \tag{24}$$

We obtain Eq. (24) without the need for an eigenvalue analysis because the eigenvectors of six rigid-body motions are already known. For better stability, we add an infinite-frequency added mass to the both sides as follows:

$$\begin{aligned} \left\{\ddot{\alpha}^{1\sim 6}(t)\right\} = {} & \left(\boldsymbol{M}_L + \boldsymbol{M}_A(\infty)\right)^{-1} \\ & \left(\left\{f^{1\sim 6}(\ddot{u}'(t),\dot{u}'(t),u'(t),t)\right\} + \boldsymbol{M}_A(\infty)\left\{\ddot{\alpha}^{1\sim n}(t)\right\}\right) \end{aligned} \tag{25}$$

where $\boldsymbol{M}_A(\infty)$ is the matrix of the infinite-frequency added mass.

We obtain the acceleration by solving Eq. (25), and calculate the velocity and displacement vectors using the 4th-order Adams–Bashforth–Moulton method. In the rigid-body approximation, the external force consists of the linear hydrodynamic pressure, nonlinear Froude–Krylov and restoring forces, the restoring forces of soft spring and gravity, and the damping forces of soft spring and roll motions.

2.4 3D FEM with modal decomposition

If we assume the ship structure to be flexible, the number of lower modes should be larger than six in Eqs. (22) and (23). By assuming that the responses of the higher modes are quasi-static, we decompose Eq. (23) into two equations as follows:

$$\boldsymbol{M}_L\left\{\ddot{\alpha}^{1\sim n}(t)\right\}+\boldsymbol{C}_L\left\{\dot{\alpha}^{1\sim n}(t)\right\}+\boldsymbol{K}_L\left\{\alpha^{1\sim n}(t)\right\}=\left\{f^{1\sim n}(\ddot{u}'(t),\dot{u}'(t),u'(t),t)\right\} \tag{26}$$

$$\boldsymbol{K}_H\left\{\alpha^{n\sim}(t)\right\}=\left\{f^{n\sim}(\ddot{u}'(t),\dot{u}'(t),u'(t),t)\right\} \tag{27}$$

To derive Eqs. (26) and (27), we use the 3D FEM to obtain the eigenvectors and modal stiffness matrices of the flexible modes. We recalculate the eigenvectors on the grids of the panel models to estimate the external modal forces due to fluid pressures. We note that Eq. (26) couples fluid and structure with respect to springing and whipping. Eq. (27), on the other hand, is decoupled and need not be solved in seakeeping analyses. We add an infinite-frequency added mass to both sides of Eq. (26) as follows:

$$\left\{\ddot{\alpha}^{1\sim n}(t)\right\}=\left(\boldsymbol{M}_L+\boldsymbol{M}_A(\infty)\right)^{-1}\left(\left\{f^{1\sim n}(\ddot{u}'(t),\dot{u}'(t),u'(t),t)\right\}-\boldsymbol{C}_L\left\{\dot{\alpha}^{1\sim n}(t)\right\}-\boldsymbol{K}_L\left\{\alpha^{1\sim n}(t)\right\}+\boldsymbol{M}_A(\infty)\left\{\ddot{\alpha}^{1\sim n}(t)\right\}\right) \tag{28}$$

Typically, the number of lower modes is smaller than 20, which includes the global vertical bending and torsion modes. Consequently, the DOF of Eq. (28) is much smaller than that of Eq. (21). In this approach, we include a slamming load in the external force, which we obtain using the 2D GWM.

2.5 Beam representation

To model the ship structure as a beam, we used the Timoshenko beam theory because this theory produces good approximated solutions to bending problems. In recent years, a beam theory for warping-torsion has been required when modeling ship structures with large openings on the deck. In the beam representation, the ship structure is discretized into beam nodes located along the longitudinal axis. The motions on the grids of the panel models are related to the beam nodal motions via the cubic polynomials. In the same manner, the pressures of the panel modes are related to the nodal forces via the cubic polynomials. The stiffness matrix is provided by the Vlasov beam theory with 14-DOF beam elements. The two additional DOFs are related to warping. Although the structural damping matrix is modeled using Rayleigh damping, it tends to suppress rigid-body motions due to its mass matrix component.

We integrate the equation of motion in time using the Newmark-beta method, which is unconditionally stable with respect to the size of the time step. This stability is necessary for performing a direct integration because all the natural modes are included in the direct integration. We can express the acceleration and velocity of the next time step as follows:

$$\ddot{u}(t+\Delta t)=\frac{1}{\alpha\Delta t^2}\left(\boldsymbol{u}(t+\Delta t)-\boldsymbol{u}(t)\right)-\frac{1}{\alpha\Delta t}\dot{u}(t)-\left(\frac{1}{2\alpha}-1\right)\ddot{u}(t) \tag{29}$$

$$\dot{u}(t+\Delta t)=\frac{\chi}{\alpha\Delta t}\left(u(t+\Delta t)-u(t)\right)+\left(1-\frac{\chi}{\alpha}\right)\dot{u}(t)+\Delta t\left(1-\frac{\chi}{2\alpha}\right)\ddot{u}(t) \tag{30}$$

where α and χ are 0.5 and 0.25, respectively. By substituting Eqs. (29) and (30) into Eq. (21), we can express the equation of motion at the next time step as follows:

$$\left(\frac{1}{\alpha\Delta t^2}\boldsymbol{M}+\frac{\chi}{\alpha\Delta t}\boldsymbol{C}+\boldsymbol{K}\right)\boldsymbol{u}(t+\Delta t)=\boldsymbol{f}(\ddot{u}(t+\Delta t),\dot{u}(t+\Delta t),u(t+\Delta t),t+\Delta t)+\boldsymbol{M}\left[\frac{1}{\alpha\Delta t^2}u(t)+\frac{1}{\alpha\Delta t}\dot{u}(t)+\left(\frac{1}{2\alpha}-1\right)\ddot{u}(t)\right]+\boldsymbol{C}\left[\frac{\chi}{\alpha\Delta t}u(t)+\left(\frac{\chi}{\alpha}-1\right)\dot{u}(t)+\Delta t\left(\frac{\chi}{2\alpha}-1\right)\ddot{u}(t)\right] \tag{31}$$

We can solve Eq. (31) using an iterative sequence because of the external force term on the right-hand side. We can successfully apply a fixed point iteration using an Aitken acceleration scheme. This acceleration scheme is necessary because of the impulsiveness of the added mass, the details of which can be found in the work of Kim *et al*. (2009).

3 Numerical modeling of the 6750-TEU containership

Table 2 lists the principal dimensions of the 6750-TEU containership and that of its experimental model. The experimental model, constructed by the Korea Research Institute of Ship and Ocean Engineering (KRISO)/Korea Institute of Ocean Science and Technology, consists of an eight-segment hull and a rectangular backbone, as shown in Fig. 3. The backbone has a hollow rectangular section 200 mm wide, 50 mm high, and 2.3 mm thick (1/70 scale). We used a fixing system to connect the hull and backbone, which consists of upper and lower supporting plates, and which is expected to slightly increase the bending rigidity of the structure. We created a set of numerical models using the above model data, including a linear panel model for the boundary value problem of the 3D Rankine panel method, a nonlinear panel model for considering the nonlinear Froude–Krylov and restoring forces, a slamming model for

the water-entry event of the 2D GWM, and a structural model of the rigid-body, beam, or 3D FEM. More details can be found in the recent publication by Kim and Kim (2016).

Table 2 Principal dimensions of the 6750-TEU containership

Item	Real scale	Model scale
Scale	1/1	1/70
L_{BP}/m	286.6	4.094
Breadth/m	40	0.571
Draft at AP and FP/m	11.98	0.171
Displacement	85 562.7 t	249.454 kg
KG/m	16.562	0.237
LCG from AP/m	138.395	1.977
K_{xx}/m	14.6	0.206
K_{yy}/m	70.144	1.002
K_{zz}/m	70.144	1.002
Neutral axis/m	7.35	0.105
Wet natural frequency of two-node VB/Hz	0.645	5.396
Wet damping ratio of two-node VB/%	2.0	2.0

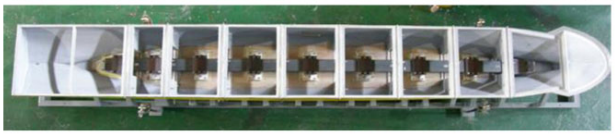

Fig. 3 Experimental model of the 6750-TEU containership

3.1 Fluid models

The hull form is described by 30 cross-section lines and two forward-perpendicular (FP) and aft-perpendicular (AP) center lines, as shown in Fig. 4. We generated the body surface using these lines and then discretized it into panels. First, we created a linear panel model by distributing 400 panels on the mean body surface and 2 500 panels on the free surface, as shown in Fig. 5. In the model, the center of buoyancy was located at (138.2 m, 0.0 m, 6.64 m) and the displacement was 85 001.7 m^3. Next, we created a nonlinear panel model using 3 000 panels for the whole body surface. Finally, we sliced the nonlinear model into 40 cross-sections for use as a slamming model, as shown in Fig. 6. We used convergence tests to determine the mesh densities.

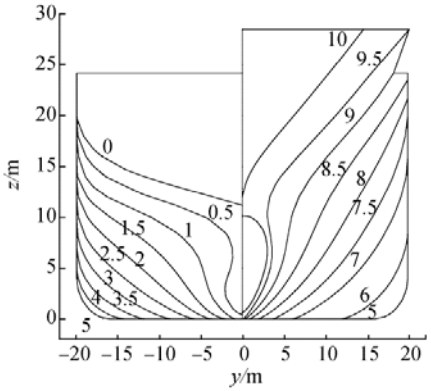

Fig. 4 Lines of the hull form

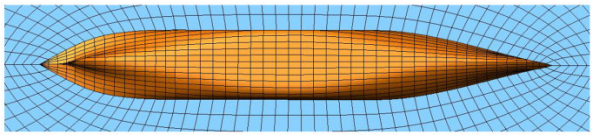

(a) Linear panel model

(b) Nonlinear body panel model

Fig. 5 Hydrodynamic panel models

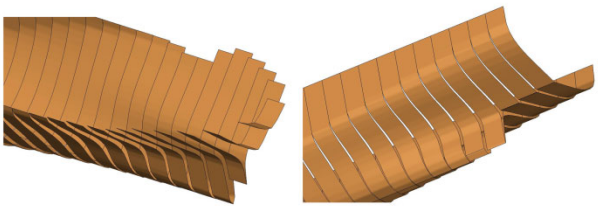

(a) FP (b) AP

Fig. 6 Vertical cross-sections of the slamming model

3.2 Structural models

Next, we generated three different structural models, as shown in Fig. 7. First, we constsructed a rigid-body model by distributing 32 lumped masses. The mass property of each segment was satisfied by four lumped masses. Then, we created a beam model using 16 beam elements and eight lumped masses. Each of the lumped masses had both translational and rotatory inertias. Lastly, we exactly reproduced the experimental model using a 3D FEM, using 55 000 shell elements to represent the backbone and hull. As in the beam model, we modeled the mass property of each segment using eight lumped masses. We extracted the eigenvectors of the 3D FEM using the fine element analysis program NASTRAN, and Fig. 8 shows the vertical bending modes. We used the beam and 3D FEMs to perform a hammering test in water for the two-node vertical bending. The natural frequencies of the two models were 0.71 Hz and 0.72 Hz, respectively, which were 10% larger than those of the experimental model. This difference might be due to the configuration of the experimental model, but as yet the reason for this is not clear. We modified the stiffnesses of the beam and 3D FEMs to obtain the natural frequencies identical to that of the experimental model.

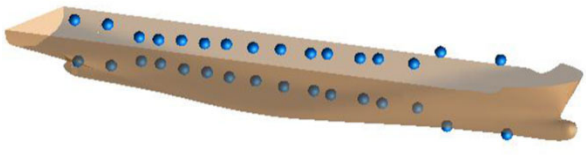

(a) Rigid-body

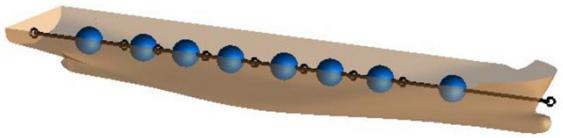

(b) Beam

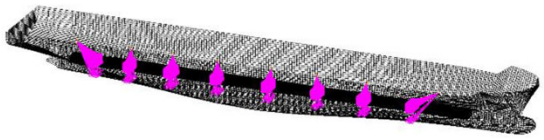

(c) 3D FEM

Fig. 7 Structural models

(a) Two-node bending

(b) Three-node bending

(c) Four-node bending

Fig. 8 Eigenvectors of vertical bending modes

4 Comparison of results

We performed a computation in the head-sea test conditions given in Table 3, where λ is the wave length, L is the ship length, and H is the wave height. These conditions consist of one linear response and three nonlinear responses. We compared three items in the response amplitude operators (RAOs) of heave, pitch, and vertical bending moment at x = 112.97 m (VBM4). In addition to these three items, we compared the longitudinal distributions of the sagging and hogging moments in the nonlinear results. Although we did not include the still-water load in the results, the motions and loads can have mean values due to the forward speed effect or nonlinear excitations of sagging and hogging.

Table 3 Test conditions for benchmark test

Test ID	λ/L	H/λ	Froude No.
RAO	0.54~3.68	small value	0
NL1	1.07	1/50	0.05
NL2	1.07	1/28	0.05
NL3	1.07	1/50	0.12

4.1 Linear response: RAO

Figs. 9–11 compare the linear responses of the 6750-TEU containership in terms of heave, pitch, and VBM4. Our proposed models show almost the same heave, which was slightly smaller than that of the experimental model. The beam model underestimated the pitch compared to the other models, which might be due to the restoring and Rayleigh damping models. The restoring model must be improved and the Rayleigh damping model should be replaced by a damping matrix proportional only to a stiffness matrix. In the VBM4 results, all the models showed similar responses. The rigid-body approximations seem to be valid because there were no springing responses. We also compared the numerical results of 17 participants in the benchmark test (Kim and Kim, 2016) in terms of the average (Mean), standard deviation (SD), and the maximum (Max) and minimum (Min) values, which are plotted in Figs. 9–11. The results of our proposed models were similar to the average benchmark test results.

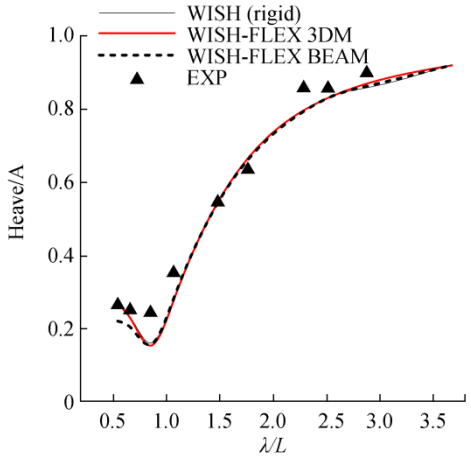

(a) Proposed method

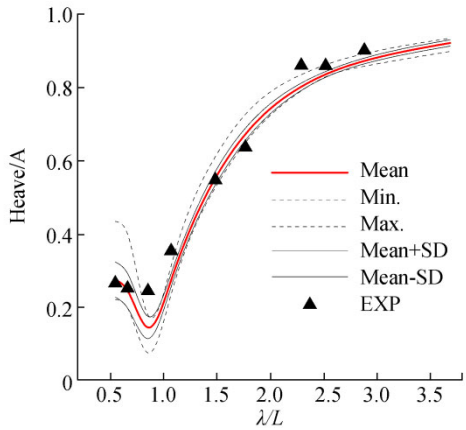

(b) Benchmark test

Fig. 9 RAOs of heave

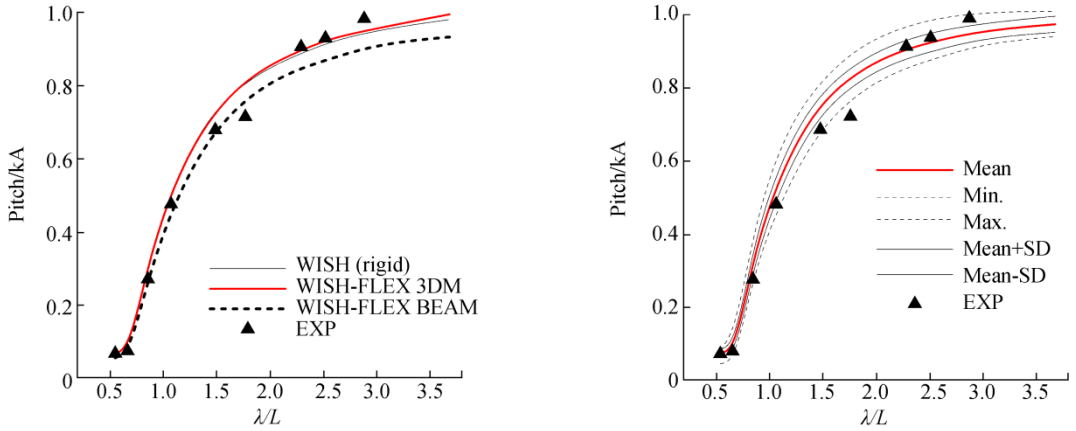

(a) Proposed method (b) Benchmark test

Fig. 10 RAOs of pitch

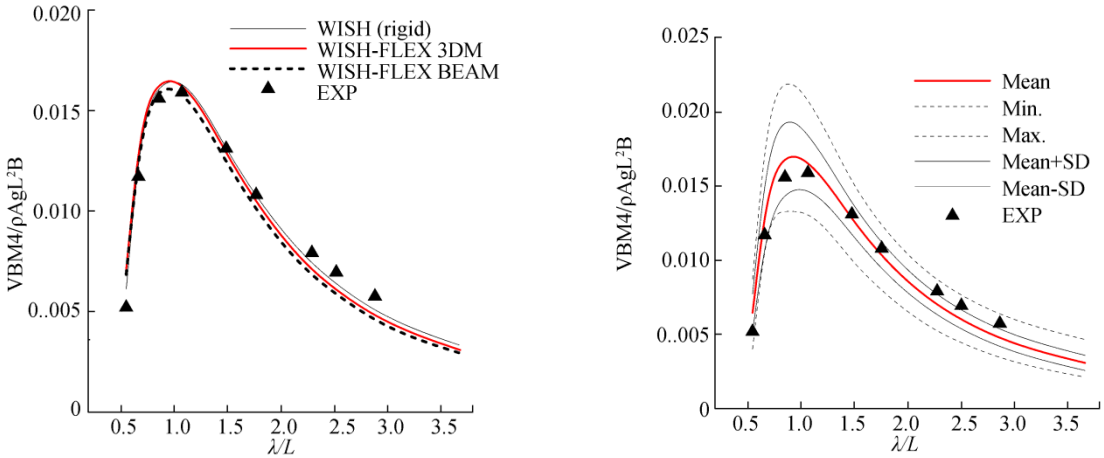

(a) Proposed method (b) Benchmark test

Fig. 11 RAOs of VB

4.2 Nonlinear response NL1

The NL1 test case was not highly nonlinear because H/λ was just 1/30. Fig. 12 shows a comparison of the time series of heave, pitch, and VBM4. We note that we shifted the time series to match the peaks of the pitch. We can observe a time lag between the numerical and experimental results, which we have also observed between other numerical and experimental results (Kim and Kim, 2016). To investigate this time lag, we must precisely measure the inertial properties of the experimental model. The time lag seemed to particularly affect the time lag of the VBM4 between the numerical and experimental results.

The numerical models tended to underestimate heave compared to the experimental model. However, the pitch was slightly overestimated in the numerical results. We found the differences between the numerical results to be negligible. Fig. 13 shows a comparison of the longitudinal distributions of VBM. We can see that the sagging moment is larger than the hogging moment due to changes in the wetted surface of the bow flare and stern. This nonlinearity was successfully considered by the weakly nonlinear approach.

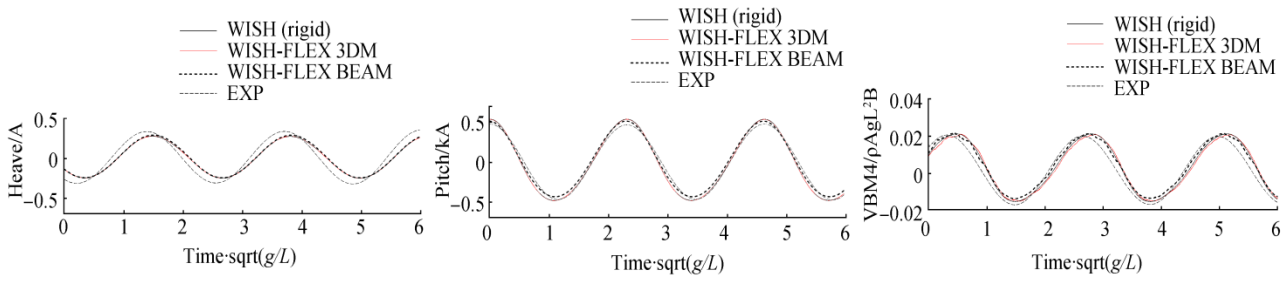

(a) Heave (b) Pitch (c) VBM4

Fig. 12 Time series in the case of NL1

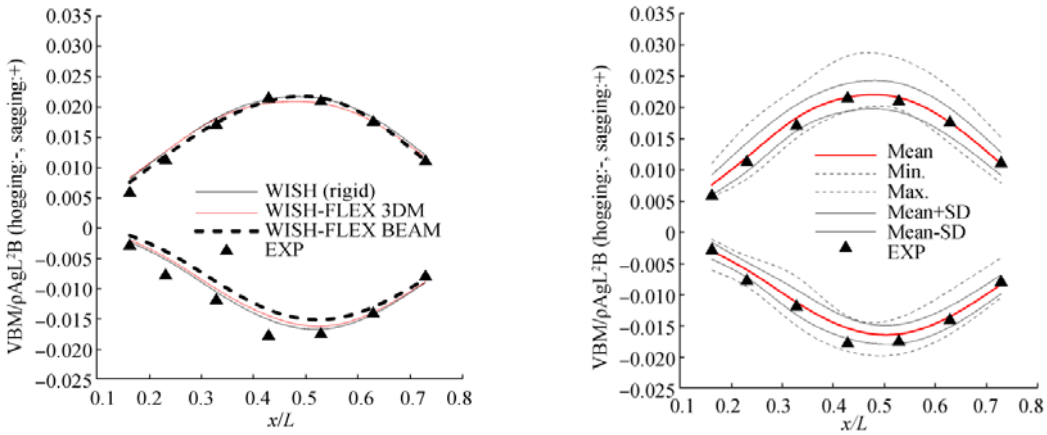

(a) Present method (b) Benchmark test

Fig. 13 Longitudinal distribution of sagging and hogging moments in the case of NL1

4.3 Nonlinear response NL2

We used the NL2 test case to simulate nonlinear springing and slamming–whipping. In the rigid-body computation, we did not consider the slamming load. However, we took it into account by using the 2D GWM in the computations of the beam and 3D FEMs. The experimental model showed a large heave compared to the numerical models, as shown in Fig. 14, but the reason for this is unclear. The rigid-body computation showed a slightly smaller heave and a slightly larger pitch than the flexible-body computations when a slamming load on the bow flare was expected.

In the VBM4 time series, in both the flexible-body computation and experiment, we observed significant high-frequency oscillations, which were due to springing and whipping. The oscillation results showed a time lag, but their magnitudes were similar. As mentioned in section 3.2, the VBM4 time lag might be due to the time lag of the heave motions. Unfortunately, it was difficult to investigate the cause of the time lags based on the available experimental data.

The 2D GWM might calculate a slamming load similar to that of the experiment. Fig. 15 shows a comparison of the longitudinal distributions of the sagging and hogging moments, both of which were significantly increased by springing and whipping. Thus, the rigid-body computation underestimated the sagging and hogging moments. The benchmark test result also revealed the difficulty in calculating the slamming and whipping due to the large SD and the far-from-average maximum and minimum values.

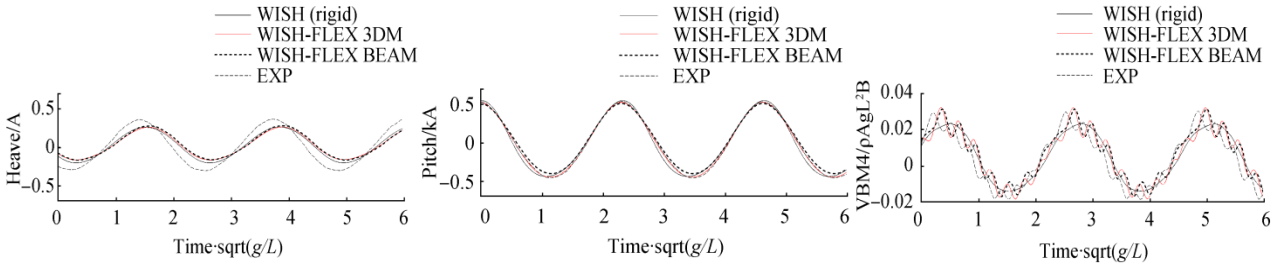

(a) Heave (b) Pitch (c) VBM4

Fig. 14 Time series in the case of NL2

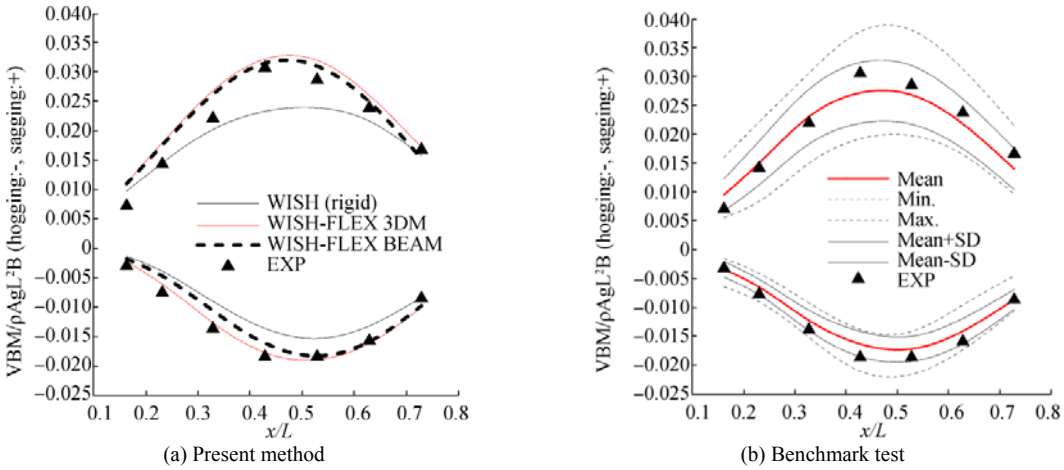

(a) Present method (b) Benchmark test

Fig. 15 Longitudinal distribution of sagging and hogging moments in the NL2case

4.4 Nonlinear response NL3

The last condition, NL3, is the same as NL1 except for forward speed. The Froude number of NL3 was 0.12, whereas that of NL1 was 0.05. Fig. 16 shows a comparison of the time series of heave, pitch, and VBM4. We can see that the experimental model showed a larger heave than the numerical models. However, the experimental and numerical models showed good agreement in pitch and VBM4. In the experimental and flexible-body VBM4 results, we an observed high-frequency components, but their magnitudes were small. As shown in Fig. 17, all the results showed good agreement with respect to the sagging and hogging moments.

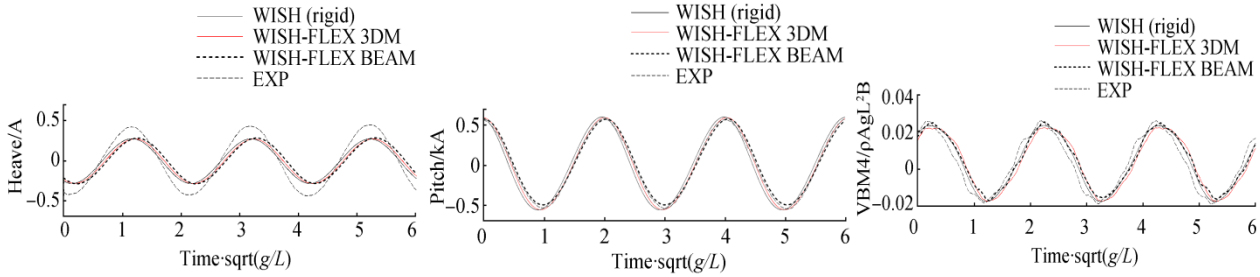

(a) Heave (b) Pitch (c) VBM4

Fig. 16 Time series of heave (top), pitch (middle), and VBM4 (bottom) in the NL3 case

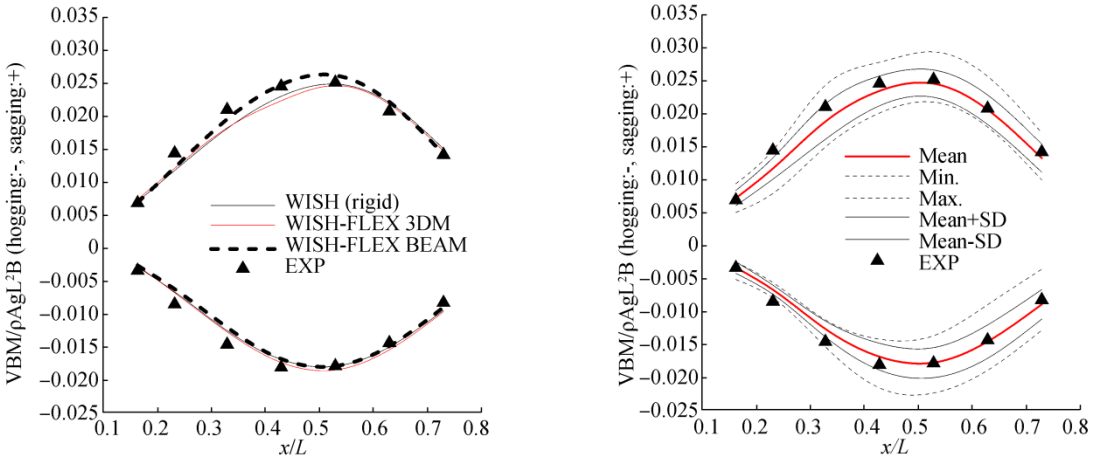

(a) Present method (b) Benchmark test

Fig. 17 Longitudinal distribution of sagging and hogging moments in the NL3 case

5 Conclusions

In this study, we applied three seakeeping analysis codes—WISH (rigid-body), WISH-FLEX BEAM, and WISH-FLEX 3DM—to the analyses of the linear and nonlinear motions and loads on the 6750-TEU containership. Based on our comparison of the computational and experimental results, we present the following findings and conclusions:

1) The hydroelastic analysis codes predicted similar results for heave, pitch, and VBM. All codes showed good agreement with the experimental measurements.

2) The results obtained with the rigid-body analysis code were almost identical to those of the hydroelastic analysis codes, except in the NL2 case.

3) In the nonlinear cases of NL1 and NL3, the sagging moments were larger than the hogging moments, which were mainly due to changes in the wetted surfaces of the bow flare and stern. We were able to successfully consider this nonlinearity using a weakly nonlinear approach.

4) Significant nonlinear springing and whipping were induced in the highly nonlinear NL2 case. The results of the flexible-body computations with the 2D GWM showed good agreement with the experimental results.

5) The experimental model showed a larger heave compared to the numerical models in the NL3 case, although the experimental and numerical results for pitch and VBM4 were similar.

Acknowledgement

This study was carried out as part of the 2nd ITTC–ISSC workshop in 2014. Special thanks to KRISO, who conducted the model test and provided the experimental results. This study was also a part of a research project supported by LRFC. (LRFC: Lloyd's Register Foundation (LRF)-funded Research Center at SNU). The support provided by LRFC is also appreciated.

References

Bishop RED, Price WG, 1979. *Hydroelasticity of ships*. Cambridge University Press, London.

Bunnik T, van Daalan E, Kapsenberg G, Shin Y, Huijsmans R, Deng G, 2010. A comparative study on state-of-the-art prediction tools for seakeeping. *Proc. 28th Symposium on Naval Hydrodynamics*, Pasadena.

Gentaz L, Guillerm PE, Alessandrini B, Delhommeau G, 1999. Three-dimensional free-surface viscous flow around a ship in forced motion. *Proc. 7th Int. Conf. Num. Ship Hydro*, Paris, 1-12.

Hirdaris SE, Temarel P, 2009. Hydroelasticity of ships - recent advances and future trends. *Proc. of the IMechE, Part M: Journal of Engineering for the Maritime Environment*, **223**(3), 305-330.
DOI: 10.1243/14750902JEME160

ITTC Seakeeping Committee, 1978. Report of the seakeeping committee. *15th Int. Towing Tank Conference*, the Hague, Netherlands, **1**, 55-114.

Jensen JJ, Dogliani M, 1996. Wave-induced ship hull vibrations in stochastic seaways, *Marine Structures*, **9**, 353-387.
DOI: 10.1016/0951-8339(95)00031-3

Khabakhpasheva TI, Kim Y, Korobkin AA, 2014. Generalized Wagner model of water impact by numerical conformal mapping, *Applied Ocean Research*, **44**, 29-38.
DOI: 10.1016/j.apor.2013.10.007

Kim JH, Kim Y, 2014. Numerical analysis on springing and whipping using fully-coupled FSI models. *Ocean Engineering*, **91**, 28-50.
DOI: 10.1016/j.oceaneng.2014.08.001

Kim JH, Kim Y, Yuck RH, Lee DY, 2015. Comparison of slamming and whipping loads by fully coupled hydroelastic analysis and experimental measurement. *Journal of Fluids and Structures*, **52**, 145-165.
DOI: 10.1016/j.jfluidstructs.2014.10.011

Kim KH, Kim Y, 2008. On technical issues in the analysis of nonlinear ship motion and structural loads in waves by a time-domain Rankine panel method. *The 23rd International Workshop on Water Waves & Floating Bodies*, Jeju.

Kim Y, Kim JH, 2016. Benchmark study on motions and loads of a 6750-TEU containership. *Ocean Engineering*, **119**, 262-273.
DOI: 10.1016/j.oceaneng.2016.04.015

Kim Y, Kim KH, Kim JH, Kim T, Seo MG, Kim Y, 2011. Time-domain analysis of nonlinear motion responses and structural loads on ships and offshore structures-development of WISH programs. *International Journal of Naval Architecture and Ocean Engineering*, **3**(1), 37-52.
DOI: 10.2478/IJNAOE-2013-0044

Kim Y, Kim KH, Kim Y, 2009. Analysis of hydroelasticity of floating ship-like structures in time domain using a fully coupled hybrid BEM-FEM. *Journal of Ship Research*, **53**(1), 31-47.
DOI: 10.3744/SNAK.2012.49.4.312

Korsmeyer FT, Lee CH, Newman JN, Sclavounos PD, 1988. The analysis of wave effects on tension-leg platforms. *Proc. 7th Conf. on Offshore Mech. and Arctic Eng,* Houston.

Korvin-Kroukovsky BV, Jacobs WR, 1957. Pitching and heaving motions of a ship in regular waves. *Trans. SNAME*, **65**, 590-632.

Kring DC, 1994. *Time domain ship motions by a three-dimensional Rankine panel method*. PhD thesis, Mass Inst. of Technology.

Lin WM, Yue DKP, 1991. Numerical solution for large-amplitude ship motions in the time domain. *Proc. 18th Symposium on Naval Hydrodynamics*, National Academy Press, Washington DC, 41-66.

Malenica S, Tuitman JT, 2008. 3D FEM-3D BEM model for springing and whipping analysis of ships. *Proc. International Conference on Design and operation of Containerships*, London.

Nakos DE, Sclavounos PD, 1990. On steady and unsteady ship wave patterns. *Journal of Fluid Mechanics*, **215**, 263-288.
DOI: 10.1017/S0022112090002646

Newman JN, 1964. A slender-body theory for ship oscillations in waves. *Journal of Fluid Mechanics*, **18**(4), 602-618.
DOI: 10.1017/S0022112064000441

Ogilvie TF, Tuck EO, 1969. *A rational strip theory of ship motions: Part I*. University of Michigan.

Sadat-Hosseini H, Wu PC, Carrica PM, Kim H, Toda Y, Stern F, 2013. CFD verification and validation of added resistance and motions of KVLCC2 with fixed and free surge in short and long head waves. *Ocean Engineering*, **59**, 240-273.
DOI: 10.1016/j.oceaneng.2012.12.016

Salvesen N, Tuck EO, Faltinsen O, 1970. Ship motions and sea loads. *Trans. SNAME*, **78**, 250-287.

Shin KH, Jo JW, Hirdaris SE, Jeong SG, Park JB, Lin F, Wang Z, White N, 2015. Two- and three-dimensional springing analysis of a 16,000 TEU container ship in regular waves. *Ships and Offshore Structures*, **10**(5), 498-509.
DOI: 10.1080/17445302.2015.1014255

Yang KK, Nam BW, Lee JH, Kim Y, 2013. Numerical analysis of large-amplitude ship motions using FV-based Cartesian grid method. *International Journal of Offshore and Polar Engineering*, **23**(3), 168-196.

Zhao R, Faltinsen O, Aarsnes J, 1996. Water entry of arbitrary two-dimensional sections with and without flow separation. *Proc. the Twenty-First Symposium on Naval Hydrodynamics*, Trondheim.